

A two-dimensional, depth-integrated model for internal wave propagation over variable bathymetry

Patrick J. Lynett, Philip L.-F. Liu*

School of Civil and Environmental Engineering, Cornell University, Ithaca, NY 14853, USA

Received 10 May 2001; accepted 2 November 2001

Abstract

Based on assumptions of an inviscid fluid and weakly rotational flow, a set of depth-averaged governing equations are developed to model long internal waves in two horizontal dimensions. These waves are assumed to be weakly nonlinear and weakly dispersive, existing in a two-layer system with a small density difference between the layers. No restriction is placed on the bathymetry or the dominant wave propagation direction. A high-order, finite difference numerical algorithm is developed, formally accurate to $(\Delta x)^4$ in space and $(\Delta t)^4$ in time. The model is checked with known analytical solutions and experimental data. Real bathymetry case studies are also performed, including simulations of internal waves evolving in the Strait of Gibraltar and near the island of Dongsha in the China Sea. Numerical results show strong similarities to satellite images taken over the same locations.

© 2002 Elsevier Science B.V. All rights reserved.

1. Introduction

The evolution of internal waves and interaction of internal waves with other waves and geological features in the horizontal plane is not well understood and has been studied to only a small degree. Most existing models include only one horizontal dimension, or are only weakly two-dimensional. Some of the earliest work made use of the Korteweg de Vries (KdV) equation [1], which is applicable to uni-directional waves. Many others have made use of the KdV-type equations, including Lee and Beardsley [2], Farmer [3], Maxworthy [4], Apel et al. [5], and Liu [6], adding modifications, such as dissipation and shoaling effects, to make the equation more applicable to real oceanographic situations.

An approach that does include two horizontal dimension effects, however only weakly, is the Kadomtsev and Petviashvili (K–P)-type equations. These equations have been utilized recently [7–9], applied to situations such as wave propagation through a narrow channel. The K–P equation requires that the spatial variation of the waveform in the transverse direction is small compared with that along the direction of wave propagation.

Recently, more advanced models have been developed [10,11], but these too are limited to one horizontal dimension or only include weak two-dimensional effects. When attempting to model internal wave evolution over real topography, interaction with islands or other geologic features, a fully two-dimensional model is needed. Observations by Liu et al. [12] in the China Sea clearly indicate strong two-dimensional wave–wave interactions and the diffraction and refraction of internal waves by bathymetry and islands.

* Corresponding author. Tel.: +1-607-255-3438; fax: +1-607-255-9004.
E-mail address: pll3@cornell.edu (Philip L.-F. Liu).

In this paper, based on a two-layer fluid system with a small density difference between the layers, a model for internal wave propagation on the horizontal plane is presented. The model incorporates both weakly nonlinear and dispersive effects. A high-order numerical algorithm is then developed, using a form similar to that proposed by Wei and Kirby [13]. Validation of the numerical algorithm is performed by comparing numerical results with existing analytical solutions and experimental data. The model is also used to simulate internal waves propagating in the Strait of Gibraltar and in the vicinity of Dongsha Island in the south China Sea. Numerical results show strong similarities to satellite images taken over the same locations.

2. Governing equations and boundary conditions

The primitive governing equations for internal long waves, propagating in a two-layer fluid system with a free ocean surface, are presented in this section. The basic physical setup of the model is shown in Fig. 1. The interfacial displacement is represented by η' (defined as positive upward), the small free surface displacement by ζ' , the undisturbed upper and lower layer thicknesses by h'_1 and h'_2 , and the upper and lower layer densities by ρ'_1 and ρ'_2 . Note h'_1 is constant, but h'_2 varies in space. For internal long waves, the linear phase speed is given as (e.g. see [10])

$$c_0^2 = \frac{gh'_1h'_2(\rho'_2 - \rho'_1)}{\rho'_2h'_1 + \rho'_1h'_2}. \tag{1}$$

For

$$\frac{\rho'_2 - \rho'_1}{\rho'_2} = \frac{\Delta\rho'}{\rho'_2} \ll 1, \tag{2}$$

the phase speed can be approximated as

$$c_0^2 \cong g \frac{\Delta\rho'}{\rho_0} \frac{h'_1h'_2}{h'_1 + h'_2} = g^*h_0, \tag{3}$$

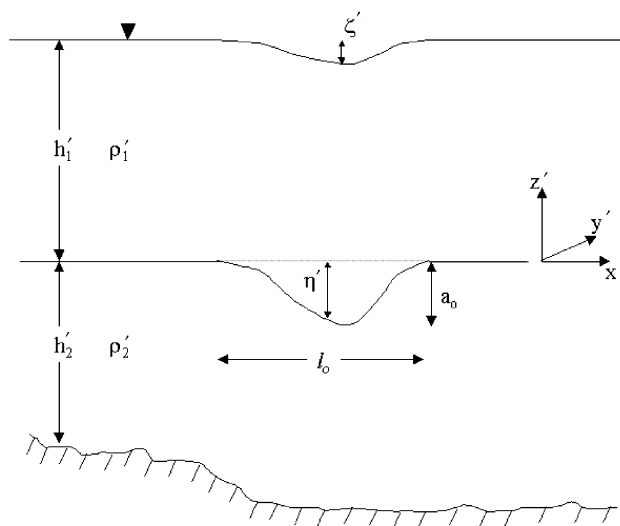


Fig. 1. Basic formulational setup.

where

$$g^* = g \frac{\Delta\rho'}{\rho_0}, \tag{4}$$

$$h_0 = \frac{h'_1 h'_2}{h'_1 + h'_2}, \tag{5}$$

$$\rho_0 = \rho'_2, \tag{6}$$

and g is the gravity. Therefore, dispersive effects will be governed by the characteristic water depth, h_0 . The characteristic length of the wave motion ℓ_0 is the horizontal length scale, $\ell_0/\sqrt{g^* h_0}$ is the time scale, and the characteristic wave amplitude a_0 is the scale of wave motion. With these scales, we can define the following dimensionless variables:

$$\begin{aligned} (x, y) &= \frac{(x', y')}{\ell_0}, & z &= \frac{z'}{h_0}, & t &= \frac{\sqrt{g^* h_0} t'}{\ell_0}, & \eta &= \frac{\eta'}{a_0}, & \Delta\rho &= \frac{\Delta\rho'}{\rho_0}, \\ (h_1, h_2) &= \frac{(h'_1, h'_2)}{h_0}, & \zeta &= \frac{\zeta'}{a_0 \Delta\rho}, & (p_1, p_2) &= \frac{(p'_1, p'_2)}{\rho_0 g^* a_0}, & (\rho_1, \rho_2) &= \frac{(\rho'_1, \rho'_2)}{\rho_0}, \\ (U, V, u, v) &= \frac{(U', V', u', v')}{\varepsilon \sqrt{g^* h_0}}, & (W, w) &= \frac{(W', w')}{(\varepsilon/\mu) \sqrt{g^* h_0}}, \end{aligned} \tag{7}$$

in which the symbol prime ($'$) denotes dimensional quantities, (U, V, u, v) represents the dimensionless horizontal velocity components in the upper and lower layers, (W, w) the dimensionless vertical velocity components in the upper and lower layers, and (p_1, p_2) represents the dimensionless dynamic pressures. The scale for ζ , the free surface displacement, is much smaller than that for the interfacial wave displacement (e.g. see [14]). Two dimensionless parameters have been introduced above, which are

$$\varepsilon = \frac{a_0}{h_0}, \quad \mu = \frac{h_0}{\ell_0}. \tag{8}$$

It should be noted that in the following analysis, both ε and μ are considered as small parameters. More specifically, the relationship between nonlinearity and frequency dispersion is assumed to be

$$O(\varepsilon^3) = O(\mu^4) \ll 1. \tag{9}$$

This assumption allows one to examine large amplitude internal waves. Naturally, this assumption will lead to a set of model equations that contain, as subsets, equations of lower order in ε , such as that for the typical long wave expansion, $O(\varepsilon) = O(\mu^2)$. Furthermore, the scaled density difference between the layers, $\Delta\rho$, will be assumed to have a very small value, i.e. $\Delta\rho = O(\mu^4) \ll 1$, which is consistent with the Boussinesq approximation.

Assuming that the viscous effects are insignificant, the wave motion can be described by the continuity equation and Euler's equations in both the upper and lower layers. In the upper layer, i.e. $\varepsilon\eta < z < h_1 + \varepsilon \Delta\rho \zeta$, the primitive governing equations are in the following dimensionless form:

$$\mu^2 \nabla \cdot \mathbf{U} + W_z = 0, \tag{10}$$

$$\mathbf{U}_t + \varepsilon \mathbf{U} \cdot \nabla \mathbf{U} + \frac{\varepsilon}{\mu^2} W \mathbf{U}_z = -\frac{1}{\rho_1} \nabla p_1, \tag{11}$$

$$\varepsilon W_t + \varepsilon^2 \mathbf{U} \cdot \nabla W + \frac{\varepsilon^2}{\mu^2} W W_z = -\frac{\varepsilon}{\rho_1} p_{1z}. \tag{12}$$

In the lower layer, i.e. $-h_2 < z < \varepsilon\eta$, the dimensionless primitive governing equations become

$$\mu^2 \nabla \cdot \mathbf{u} + w_z = 0, \quad (13)$$

$$\mathbf{u}_t + \varepsilon \mathbf{u} \cdot \nabla \mathbf{u} + \frac{\varepsilon}{\mu^2} w \mathbf{u}_z = -\frac{1}{\rho_2} \nabla p_2, \quad (14)$$

$$\varepsilon w_t + \varepsilon^2 \mathbf{u} \cdot \nabla w + \frac{\varepsilon^2}{\mu^2} w w_z = -\frac{\varepsilon}{\rho_2} p_{2z}, \quad (15)$$

where $\nabla = (\partial/\partial x, \partial/\partial y)$ is the horizontal gradient vector, and the subscript the partial derivative.

On the free surface, $z = h_1 + \varepsilon \Delta\rho \zeta$, the kinematic boundary condition requires

$$W = \mu^2 \Delta\rho (\zeta_t + \varepsilon \mathbf{U} \cdot \nabla \zeta) \quad \text{on } z = h_1 + \varepsilon \Delta\rho \zeta. \quad (16)$$

The dynamic free surface condition demands that the total pressure vanishes, i.e.

$$p_1 = \rho_1 \zeta \quad \text{on } z = h_1 + \varepsilon \Delta\rho \zeta. \quad (17)$$

Along the fluid interface, $z = \varepsilon\eta(x, y, t)$, the pressure is continuous, i.e.

$$p_2 = p_1 + \eta \quad \text{on } z = \varepsilon\eta, \quad (18)$$

and the kinematic boundary condition requires

$$W = \mu^2 (\eta_t + \varepsilon \mathbf{U} \cdot \nabla \eta) \quad \text{on } z = \varepsilon\eta, \quad (19)$$

$$w = \mu^2 (\eta_t + \varepsilon \mathbf{u} \cdot \nabla \eta) \quad \text{on } z = \varepsilon\eta. \quad (20)$$

The above two expressions can be combined to give

$$W - \mu^2 \varepsilon \mathbf{U} \cdot \nabla \eta = w - \mu^2 \varepsilon \mathbf{u} \cdot \nabla \eta \quad \text{on } z = \varepsilon\eta. \quad (21)$$

At the seafloor, $z = -h_2$, the no-flux boundary condition requires

$$w = -\mu^2 \mathbf{u} \cdot \nabla h_2 \quad \text{on } z = -h_2. \quad (22)$$

The exact forms of continuity, written in terms of the depth-averaged horizontal velocity, can be easily derived at this point. Integration of (13) from $-h_2$ to $\varepsilon\eta$, with the application of boundary conditions (20) and (22) yields

$$\eta_t + \nabla \cdot [(h_2 + \varepsilon\eta)\bar{\mathbf{u}}] = 0. \quad (23)$$

For the upper layer, the procedure is the same. Integration of (10) from $\varepsilon\eta$ to $h_1 + \varepsilon \Delta\rho \zeta$, with the application of boundary conditions (20) and (22) gives

$$\eta_t - \nabla \cdot [(h_1 - \varepsilon\eta)\bar{\mathbf{U}}] = \mathcal{O}(\Delta\rho), \quad (24)$$

where

$$\bar{\mathbf{u}} = \frac{1}{h_2 + \varepsilon\eta} \int_{-h_2}^{\varepsilon\eta} \mathbf{u} \, dz, \quad (25)$$

$$\bar{\mathbf{U}} = \frac{1}{h_1 - \varepsilon\eta} \int_{\varepsilon\eta}^{h_1} \mathbf{U} \, dz, \quad (26)$$

are the depth-averaged horizontal velocity vectors in the lower and upper layers, respectively.

The approximate forms of the depth-integrated momentum equations are derived using a perturbation approach. A detailed derivation of these equations is included in [Appendix A](#). Using μ^2 as the small parameter, the dimensionless physical variables are expanded as power series of μ^2 . Based on the assumption that $\mathcal{O}(\varepsilon^3) = \mathcal{O}(\mu^4) \ll 1$, a

two-component vector equation results for both the upper and lower layers. The volume flux in the upper and lower layers must be equated as follows:

$$(h_1 - \varepsilon\eta)\bar{\mathbf{U}} = -(h_2 + \varepsilon\eta)\bar{\mathbf{u}} + \mathcal{O}(\Delta\rho) = \mathbf{M}, \quad (27)$$

which is the direct result of (23) and (24). With the assumption that the density difference between the two layers is very small, i.e. $\Delta\rho = \mathcal{O}(\mu^4)$, the depth-averaged momentum equation can be expressed in terms of \mathbf{M} (see Appendix A):

$$\begin{aligned} \mathbf{M}_t + \left(\frac{1}{h_1} + \frac{1}{h_2}\right)^{-1} \nabla\eta + \varepsilon \left(\frac{1}{h_1} - \frac{1}{h_2}\right) [\mathbf{M} \cdot \nabla\mathbf{M} - (\mathbf{M}\eta)_t] - \varepsilon \frac{1}{h_1^3} \left(\frac{1}{h_1} + \frac{1}{h_2}\right)^{-1} [(\mathbf{M} \cdot \nabla h_2)\mathbf{M}] \\ + \varepsilon^2 \left(\frac{1}{h_1^2} - \frac{1}{h_2 h_1} + \frac{1}{h_2^2}\right) [(\mathbf{M}\eta^2)_t - (\mathbf{M} \cdot \nabla)(\eta\mathbf{M}) - \eta(\mathbf{M} \cdot \nabla)\mathbf{M}] + \mu^2 \frac{h_1 h_2}{3} \nabla(\nabla \cdot \mathbf{M}_t) \\ - \mu^2 \left(\frac{1}{h_1} + \frac{1}{h_2}\right)^{-1} [(\nabla \cdot \mathbf{M}_t)\nabla \cdot h_2 - \frac{2}{h_2}(\mathbf{M}_t \cdot \nabla h_2)\nabla h_2 + \nabla(\mathbf{M}_t \cdot \nabla h_2)] = \mathcal{O}(\varepsilon\mu^2). \end{aligned} \quad (28)$$

Note that the momentum flux associated with the change in the free ocean surface, ζ , disappears (see Eqs. (A.28)–(A.32)). Therefore, the variation of the free surface caused by the internal wave propagation has no effect on the internal wave itself, to the order of the derived model equations. Conservation of mass, when expressed in volume flux, simply becomes

$$\eta_t + \nabla \cdot \mathbf{M} = \mathcal{O}(\mu^4). \quad (29)$$

Eqs. (28) and (29) constitute the model equations for internal wave propagation in two horizontal dimensions. The momentum equation can be written in a different form with the aid of the continuity equation. For instance, if the continuity equation is used to rewrite the nonlinear cubic and quadratic time derivatives in the momentum equation (28), the following x - and y -component momentum equations can be obtained:

$$C_{X0}P_t + C_1\eta_x + F^{\star} + (F_1 + C_6P_{xx})_t = \mathcal{O}(\varepsilon\mu^2), \quad (30)$$

$$C_{Y0}Q_t + C_1\eta_y + G^{\star} + (G_1 + C_6Q_{yy})_t = \mathcal{O}(\varepsilon\mu^2), \quad (31)$$

where P is the x -component of the volume flux vector \mathbf{M} , Q is the y -component, and

$$C_{X0} = 1 - \eta C_2 + \eta^2 C_4 + h_{2xx} C_7 + h_{2x}^2 C_8, \quad (32)$$

$$\begin{aligned} F^{\star} = C_2[2PP_x - (QP)_y] + C_3(P^2 h_{2x} + PQh_{2y}) + C_4[-2\eta QP_x - 2\eta PQ_y - (\eta P^2)_x - 2\eta QP_y - PQ\eta_y] \\ + C_5(\eta P^2 h_{2x} + \eta PQh_{2y}), \end{aligned} \quad (33)$$

$$F_1 = C_6(Q_{xy}) + C_8(Qh_{2x}h_{2y}) + C_7(P_x h_{2x} + Q_y h_{2x} + P_y h_{2x} + Q_x h_{2y} + Qh_{2xy}), \quad (34)$$

$$C_{Y0} = 1 - \eta C_2 + \eta^2 C_4 + h_{2yy} C_7 + h_{2y}^2 C_8, \quad (35)$$

$$\begin{aligned} G^{\star} = C_2[2QQ_y - (QP)_x] + C_3(Q^2 h_{2y} + PQh_{2x}) + C_4[-2\eta QP_x - 2\eta QQ_y - (\eta Q^2)_y - 2\eta PQ_x - PQ\eta_x] \\ + C_5(\eta Q^2 h_{2y} + \eta PQh_{2x}), \end{aligned} \quad (36)$$

$$G_1 = C_6(P_{xy}) + C_8(Ph_{2x}h_{2y}) + C_7(Q_y h_{2y} + P_x h_{2y} + P_y h_{2x} + Q_x h_{2x} + Ph_{2xy}), \quad (37)$$

$$\begin{aligned}
C_1 &= \left(\frac{1}{h_2} + \frac{1}{h_1} \right)^{-1}, & C_2 &= \varepsilon \left(\frac{1}{h_2} - \frac{1}{h_1} \right), & C_3 &= -\varepsilon \frac{1}{h_1^3} \left(\frac{1}{h_2} + \frac{1}{h_1} \right)^{-1}, \\
C_4 &= \varepsilon^2 \left(\frac{1}{h_2^2} - \frac{1}{h_2 h_1} + \frac{1}{h_1^2} \right), & C_5 &= \varepsilon^2 \frac{3}{h_2^4} \left(\frac{1}{h_2} + \frac{1}{h_1} \right)^{-1}, & C_6 &= -\mu^2 \frac{h_1 h_2}{3}, \\
C_7 &= -\frac{\mu^2}{6} \left(\frac{1}{h_2} + \frac{1}{h_1} \right)^{-1}, & C_8 &= -C_7 \frac{2}{h_2}.
\end{aligned} \tag{38}$$

This rewriting of some of the time derivatives is done because it is numerically more convenient to treat spatial derivatives than mixed time and space derivatives. The above equations reduce to those derived by Tomasson and Melville [8] for constant water depth. It should be noted, however, that Tomasson and Melville's derivation differs significantly from the one given in Appendix A, which can be straightforwardly extended to fully-nonlinear wave propagation. Also, all of Tomasson and Melville's analysis of their derived equations make the simplifying assumption of weakly two-dimensional waves, while the present model is fully two-dimensional.

3. Numerical model

The numerical scheme employs a high-order predictor–corrector scheme. Similar methods have been successfully employed by Wei and Kirby [13] and Lynett et al. [15] for modeling surface wave phenomena. The scheme makes use of centered finite differencing to fourth-order accuracy $(\Delta x)^4$, thereby minimizing numerical truncation errors in the spatial derivatives. The time and spatial variables are discretized as $t = n \Delta t$, $x = i \Delta x$, and $y = j \Delta y$. The predictor step is the third-order explicit Adams–Bashforth method [16]:

$$\eta_{i,j}^{n+1} = \eta_{i,j}^n - \left[\frac{\Delta t}{12} (23E^n - 16E^{n-1} + 5E^{n-2}) \right]_{i,j}, \tag{39}$$

$$\begin{aligned}
P_{i,j}^{n+1} &= P_{i,j}^n - \left[\frac{\Delta t}{12} (23F^n - 16F^{n-1} + 5F^{n-2}) + (2F_p^n - 3F_p^{n-1} + F_p^{n-2}) \right. \\
&\quad \left. + (C_{XO}^n - 1)(2P^n - 3P^{n-1} + P^{n-2}) \right]_{i,j},
\end{aligned} \tag{40}$$

$$\begin{aligned}
Q_{i,j}^{n+1} &= Q_{i,j}^n - \left[\frac{\Delta t}{12} (23G^n - 16G^{n-1} + 5G^{n-2}) + (2G_p^n - 3G_p^{n-1} + G_p^{n-2}) \right. \\
&\quad \left. + (C_{YO}^n - 1)(2G^n - 3G^{n-1} + G^{n-2}) \right]_{i,j},
\end{aligned} \tag{41}$$

where

$$E = P_x + Q_y, \tag{42}$$

$$F = C_1 \eta_x + F^{\star}, \tag{43}$$

$$F_p = F_1 + F_2, \tag{44}$$

$$F_2 = C_6 P_{xx}, \tag{45}$$

$$G = C_1 \eta_y + G^{\star}, \tag{46}$$

$$G_P = G_1 + G_2, \tag{47}$$

$$G_2 = C_6 Q_{yy}, \tag{48}$$

where all time and spatial step subscripts have been dropped (but all terms are evaluated at the same space and time step).

With the predicted values of $\eta_{i,j}^{n+1}$, $P_{i,j}^{n+1}$, and $Q_{i,j}^{n+1}$ the fourth-order Adams–Moulton scheme is adapted for the iterative corrector stage [16]:

$$\eta_{i,j}^{n+1} = \eta_{i,j}^n - \left[\frac{\Delta t}{24} (9E^{n+1} + 19E^n - 5E^{n-1} + E^{n-2}) \right]_{i,j}, \tag{49}$$

$$P_{i,j}^{n+1} = P_{i,j}^n - \left[\frac{(\Delta t/24)(9F^{n+1} + 19F^n - 5F^{n-1} + F^{n-2}) + (F_C^{n+1} - F_C^n)}{C_{XO}^{n+1} - C_6(30/(12\Delta x^2))} \right]_{i,j}, \tag{50}$$

$$Q_{i,j}^{n+1} = Q_{i,j}^n - \left[\frac{(\Delta t/24)(9G^{n+1} + 19G^n - 5G^{n-1} + G^{n-2}) + (G_C^{n+1} - G_C^n)}{C_{YO}^{n+1} - C_6(30/(12\Delta y^2))} \right]_{i,j}, \tag{51}$$

where

$$F_C = F_1 + F_3, \tag{52}$$

$$F_3 = C_6 \frac{-P_{i+2,j}^n + 16P_{i+1,j}^n + 16P_{i-1,j}^n - P_{i-2,j}^n}{12\Delta x^2}, \tag{53}$$

$$G_C = G_1 + G_3, \tag{54}$$

$$G_3 = C_6 \frac{-Q_{i,j+2}^n + 16Q_{i,j+1}^n + 16Q_{i,j-1}^n - Q_{i,j-2}^n}{12\Delta y^2}. \tag{55}$$

The corrector step is iterated if the absolute error in η , P , or Q at any grid point is greater than 10^{-6} . For small nonlinearity, $\varepsilon < 0.1$, the corrector step typically requires eight or less iterations. As nonlinearity increases, however, so do the required iterations; a numerical run with $\varepsilon = 0.3$ may require 20 iterations before satisfying the convergence criterion.

4. Boundary conditions

For a solid boundary with outward normal vector \vec{n} , the kinematic boundary condition is given as

$$\mathbf{M} \cdot \vec{n} = 0 \text{ along the wall.} \tag{56}$$

With the kinematic property, the momentum equation (28), requires that

$$\nabla \eta \cdot \vec{n} = O(\varepsilon, \mu^2) \text{ along the wall.} \tag{57}$$

Note that when the boundary wall is a straight line, i.e. $\nabla \cdot \vec{n} = 0$, which will always be the case in the results presented in this paper, (57) satisfies the nonlinear terms in (28), i.e. $\nabla \eta \cdot \vec{n} = O(\mu^2)$. To simplify the numerical implementation of the above boundary condition (57), the normal gradient of the free surface is set to zero. Therefore, it must be noted that the reflective wall boundary condition satisfies a low-order (in μ^2) version of the model momentum equation (28). For the two-dimensional problem, the following additional condition is required:

$$\frac{\partial M_T}{\partial n} = O(\varepsilon, \mu^2) \text{ along the wall,} \tag{58}$$

where M_T is the tangential flux component along the boundary. This condition can be found by examination of the linear, nondispersive form of the tangential-flux momentum equation, along with substitution of (57). To simplify the numerical implementation of the above boundary condition (58), the normal gradient of the tangential flux is set to zero. Note that the boundary conditions (57) and (58) are required due to the second-order spatial derivatives included in the model equations (28) and (29). The above three conditions form a complete set of boundary conditions for a solid wall.

It is also desirable to be able to implement an open, or radiation, boundary condition, allowing the waves to propagate through the boundary and exit the computational domain. The low-order radiation condition employed here has been used successfully by Wang [17] in a similar scheme, and is given as

$$\frac{\partial R}{\partial t} \mp c \frac{\partial R}{\partial n} = 0 \text{ along the boundary,} \quad (59)$$

where R is any variable η , P , or Q , and c is the wave celerity. In nondimensional terms, the celerity is set equal to 1. Recent work done on the subject of radiation conditions would show this description to be simplistic, but the numerical application of (59) yields acceptable results. It should also be noted that there was always a small reflection off these boundaries, on the order of 5% of the incident wave height. This type of reflection is acceptable for most cases where single soliton evolution is modeled, but for cases with continuous wave trains, the small reflections accumulate and will eventually destroy the simulation. For these simulations a different boundary condition is required, such as a sponge layer. Sponge layers can damp out a wide range of frequencies, but typically need to be a couple of wavelengths wide Wei and Kirby [13], thereby requiring additional computational resources.

When the radiation conditions are applied the solution on the boundary would tend to oscillate around the eventual solution during the iterative corrector stage. This oscillation would occasionally prevent the solution from converging. To eliminate this problem, an over-relaxation technique was implemented near the open boundaries. The over-relaxation expression is

$$R = (1 - \delta)R_c + \delta R_p, \quad (60)$$

where δ is the over-relaxation coefficient between 0 and 1, R_c the variable, either η , P , or Q , from the current iteration, and R_p is the variable from the previous iteration. A δ value of 0.45 gave good results on all numerical runs.

5. Model validation

The first check on the numerical model is to make certain that mass is conserved. The procedure for checking mass is as follows: a solitary wave was placed in a domain with bathymetry profile that varied in both the x - and y -directions. All of the numerical boundaries are solid wall boundaries. Simulations were run for various ε and h_2/h_1 combinations. For mass conservation, it is required that

$$\frac{\partial}{\partial t} \int_{\text{length}} \int_{\text{width}} \eta \, dx \, dy = 0. \quad (61)$$

Typical grid spacing of $\Delta x = \Delta y = 0.025$ (corresponding to 40 grid points per wavelength) and $\Delta t = 0.01$ were used for these and all other simulations described in this paper. For all simulations, mass was conserved to within 0.5% of the initial mass.

The second check of the model is to make certain that permanent solutions, in the analytical sense, must also remain numerically permanent. Two permanent solutions to our two-layer model will be examined: a solitary wave and a monotonic bore. The solitary wave examined here is a solution to the equations without cubic nonlinearity and with constant depth. The solitary wave has the familiar dimensionless form

$$\eta = \text{sech}^2 \left(\frac{x - ct}{l} \right), \quad (62)$$

where

$$c = 1 + \frac{\varepsilon(h_2 - h_1)}{2h_1h_2}, \quad (63)$$

$$l = \frac{2h_1h_2}{\sqrt{3\varepsilon(h_2 - h_1)}}. \quad (64)$$

The above soliton solution can be derived from the model equations (28) and (29) for the constant water depth case [18]. A solitary wave of modest nonlinearity, $\varepsilon = 0.2$, propagating through layers of constant thickness was run to test for permanency. To make sure that the cubic nonlinearity had no effect on the solution, these terms are neglected for this simulation. A lower to upper water depth ratio of 2.0 is used. The wave was allowed to propagate for 15 wavelengths, resulting in no change in form. The numerical waveform after 15 wavelengths is compared to the analytical waveform in Fig. 2. Additionally, an identical simulation was performed, except that the cubic nonlinearity was not forced to zero. This waveform is also plotted in Fig. 2. Although the cubic nonlinear terms are small in magnitude, they have a clear effect on the waveform. The cubic terms disrupt the balance between nonlinearity and frequency dispersion, resulting in a deformed, nonsymmetric wave shape after 15 wavelengths of propagation.

To ensure that cubic nonlinearity is being computed correctly, we check for permanency of a monotonic bore. The bore, a permanent solution of the governing equations when cubic nonlinearity is important, has the following

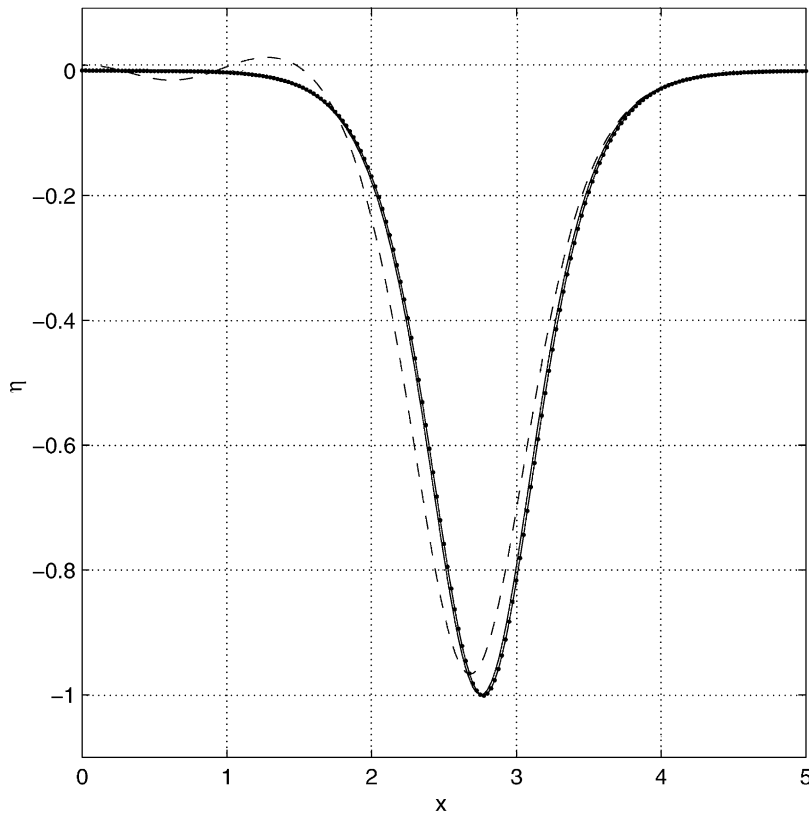


Fig. 2. Solitary waveform from analytical solution (—), numerical solution without cubic nonlinearity (---), and numerical solution with cubic nonlinearity (-·-·).

dimensionless solution [18,19]:

$$\eta = \frac{1}{2} \left[1 + \tanh \left(\frac{x - ct}{l} \right) \right], \quad (65)$$

where

$$c = 1 + \frac{d_{-2}^2}{8d_{-3}}, \quad (66)$$

$$l = \sqrt{\frac{16\mu^2 d_{-1} d_{-3}}{3d_{-2}^2}}, \quad (67)$$

and

$$d_n = h_2^n + (-1)^{n-1} h_1^n. \quad (68)$$

A numerical simulation with $\varepsilon = 0.2$ and a lower to upper water depth ratio of 1.1 was carried out. The numerical wave profile after 15 wavelengths of propagation is plotted with the analytical solution in Fig. 3, and is numerically permanent.

A frequently examined aspect of internal wave propagation is that of shoaling. The expected behavior of an internal wave of depression as it propagates into a shallower region is the decomposition into a train of oscillatory waves. This has been recorded in the field and laboratory, and a numerical simulation depicting the evolution is

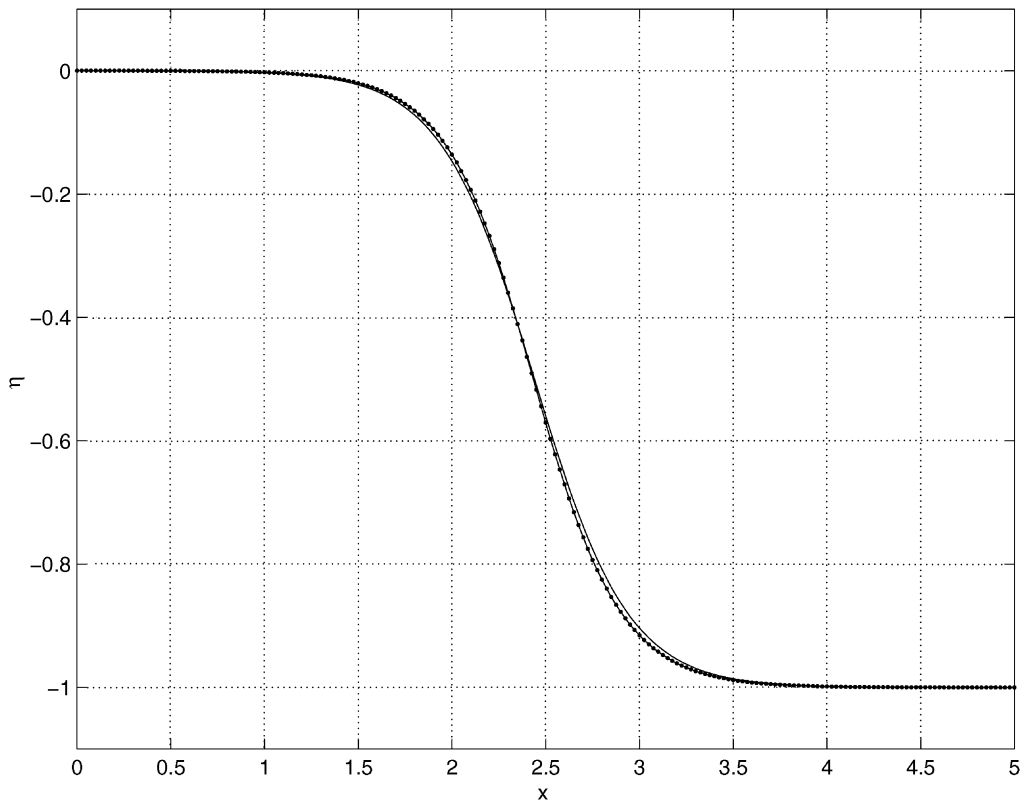


Fig. 3. Comparisons between numerical (---) and analytical (—) bore waveform.

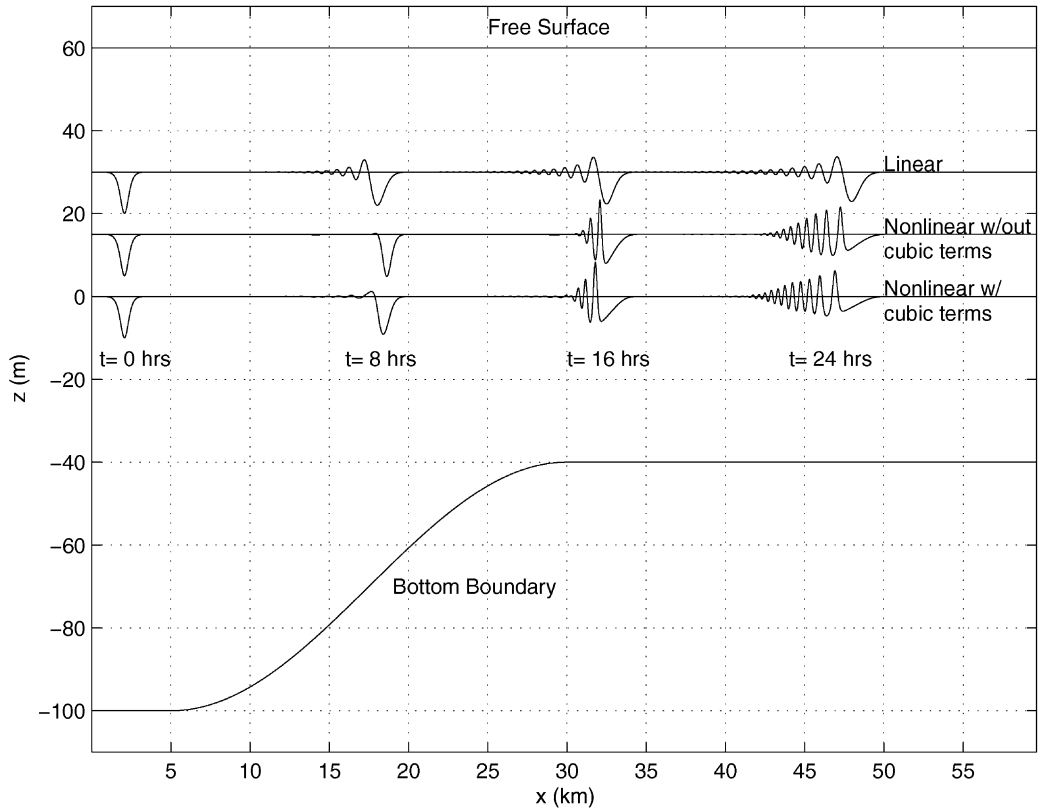


Fig. 4. Numerical simulation of an internal wave, with initial height of 10 m, evolving over a shelf. The line plotted at $z = 0$ m shows the nonlinear numerical results, the line plotted at $z = 15$ m shows the nonlinear results with cubic nonlinearity neglected, and the line plotted at $z = 30$ m indicates the linear waveform. Note that the waveforms offset from the interface ($z = 0$ m) have been manually offset for easier viewing; all results actually exist at the interface.

shown in Fig. 4. The physical parameters of the numerical simulation are taken from Liu et al. [12], and model typical internal wave shoaling off the coast of Taiwan. A solitary wave with initial amplitude of 10 m is located between a lower layer of depth 100 m and a 60 m thick upper layer. The initial nonlinearity of this wave is $\varepsilon = 0.26$. The horizontal length of the slope is 25 km, and the shelf lower layer depth is 40 m. Liu et al.'s numerical model is based on the KdV-type equation, and exhibits very similar waveform compared to the model presented here. The back face of the soliton steepens as it travels up the shelf, and after passing the shelf break it degenerates into a rank ordered series of waves.

Also shown in Fig. 4 are the numerical waveforms without cubic nonlinearity (plotted on $z = 15$ m) and without nonlinearity at all (plotted on $z = 30$ m). The linear results show a initially slower moving wave, until the critical depth is reached. Note the larger amplitude of the oscillatory trailing waves associated with the nonlinear results. The nonlinear interactions are passing energy from the primary frequency into higher frequencies. This energy transfer cannot occur with linear equations, and the result is a much less steep, smoother tail. The differences between the nonlinear results with and without cubic nonlinearity are significantly less obvious. The results with cubic nonlinearity have a slightly later arrival time that those without, and the additional nonlinearity appears to be creating a longer train of oscillatory waves behind the leading wave, due to the higher order nonlinear energy transfer. The leading wave height in the results with cubic nonlinearity is about 6% less that those without the cubic terms, due to the cubic nonlinear energy transfer into the trailing waves.

The shelf depth represents nearly the shallowest depth that this model can accommodate for this setup. If the lower layer thickness was less on the shelf, say 30 m, the waveform becomes unstable, represented by short waves created along the back face that are always $2\Delta x$ in length, regardless of the grid size. This numerical observation is consistent with reported numerical and experimental work [20,21], where it was found that for a lower layer shelf depth with $a/h_2 > 0.3$ (equal to 0.25 in this simulation), mixing along the back face of the wave occurs, due to wave breaking, as the wave reaches the shelf break. This observation indicates the practical importance of including a numerical breaking wave criteria, which is not done here.

To test the model accuracy against experiment, data is taken from Helfrich [21]. In these experiments, a solitary wave is generated and allowed to travel up a slope. The upper layer thickness is 10 cm, the initial lower layer thickness is 26 cm, and slope is 0.05, or roughly 2.5 wavelengths long. The incident wave height is 3.6 cm ($\varepsilon = 0.27$). Fig. 5 shows the time series comparisons between numerics and experiment; time is scaled by c_0/L , where L is the horizontal length of the slope. Fig. 5(a) is taken at the beginning of the slope, and is essentially the incident wave condition. The time series shown in Fig. 5(b) is at a location $2/3$ up the slope. Both numerical and experimental waves show a clear shoaled form, with an increased amplitude and steepened back face. The numerical wave reaches the location slightly faster, and has a slightly larger amplitude; a difference in the order of 10% of the experimental period and less than 5% of the wave height. The larger amplitude in the numerical simulation is most likely due to the exclusion of dissipative effects, and the faster phase speed is probably due to the larger amplitude and the fact that the experiments are not truly a two-layer system. The experiments are performed in a stratified system with fresh and salt water, where the interfacial thickness is nearly 2 cm, and is therefore not a two-layer system. This

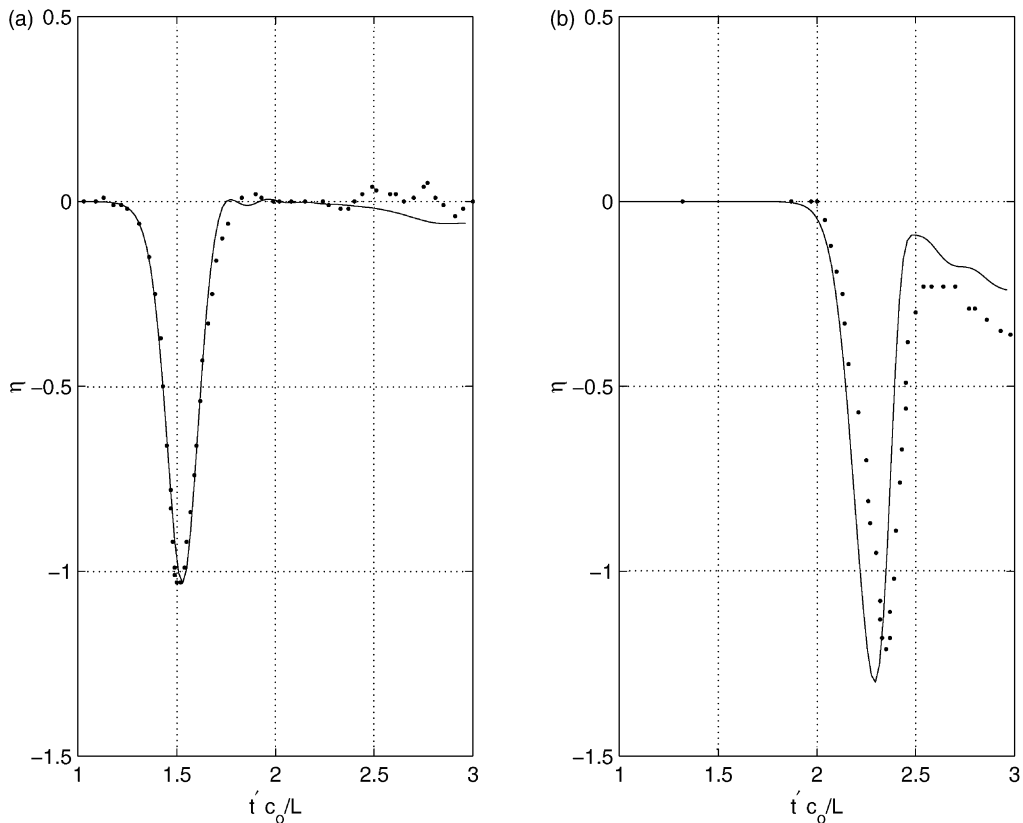


Fig. 5. Comparison between numerical (—) and experimental (· · ·) waves traveling up a slope.

comparison is meant to demonstrate the differences one might expect when using a two-layer model to simulate real oceanographic internal waves. The waveform should be very similar, but phase speeds may differ, as was demonstrated by Helfrich and Melville [20].

Model validation on two horizontal dimensions is difficult, due to a lack of two-dimensional internal wave data. Thus, the two-dimensional validation must be performed qualitatively, primarily using satellite imagery. First, we investigate possibly the most thoroughly examined internal wave location, the Strait of Gibraltar. Internal solitons, as they exit the Strait and enter the Mediterranean Sea, can have amplitudes greater than 80 m [22]. Nearly all the published field data show leading solitons with amplitudes of at least 40 m. This is unfortunate, as the present model cannot simulate a wave of this large height. In the Strait, the equivalent single layer depth, h_0 , is about 80 m. Therefore, owing to the weakly nonlinear assumption, the maximum wave height that can be modeled is approximately 25 m, and comparisons with field data will not be helpful. Admittedly, the model cannot predict the higher order nonlinearities that exist in this region, but a simulation of a smaller wave may indicate similar two-dimensional and topographic effects that can be seen in aerial imagery.

The bathymetry in the Strait was taken from the Smith and Sandwell 5 min database, and was interpolated using a bilinear routine to fit the numerical grid. Breaking and runup are not included in this model, and thus vertical walls are artificially placed along the banks of the Strait in shallow water. The walls are placed near the lower layer depth of 80 m. The lower layer depth profile is shown in Fig. 6(a). Also in this figure are the locations of the solid boundaries, shown by the gray mesh. An initial solitary wave with an amplitude of 20 m ($\varepsilon = 0.30$) is placed in the domain, located at $x = 5$ km and traveling in the positive x -direction. The lower layer depth at the initial location of the wave is 500 m, and the upper layer thickness, which is constant everywhere, is 80 m. The evolution of the wave is shown in Fig. 6(b)–(d). In Fig. 6(b), taken 4 h after the start of the simulation, the initially straight wave front is now bow-shaped as the center of the wave front, in the deepest water, travels faster than the rest of the wave. Fig. 6(c), 7 h into the simulation, shows the wave exiting the Strait, and diffracting into the open

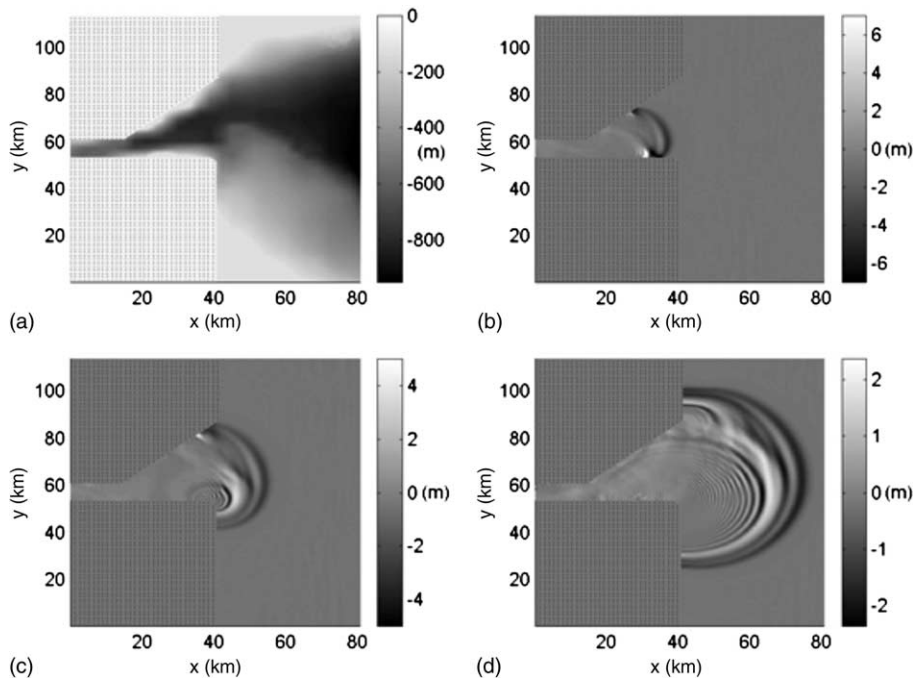


Fig. 6. Numerical simulation of internal wave passing through the Strait of Gibraltar. Plot (a) shows the lower layer depth profile, and plots (b)–(d) are successive snapshots.

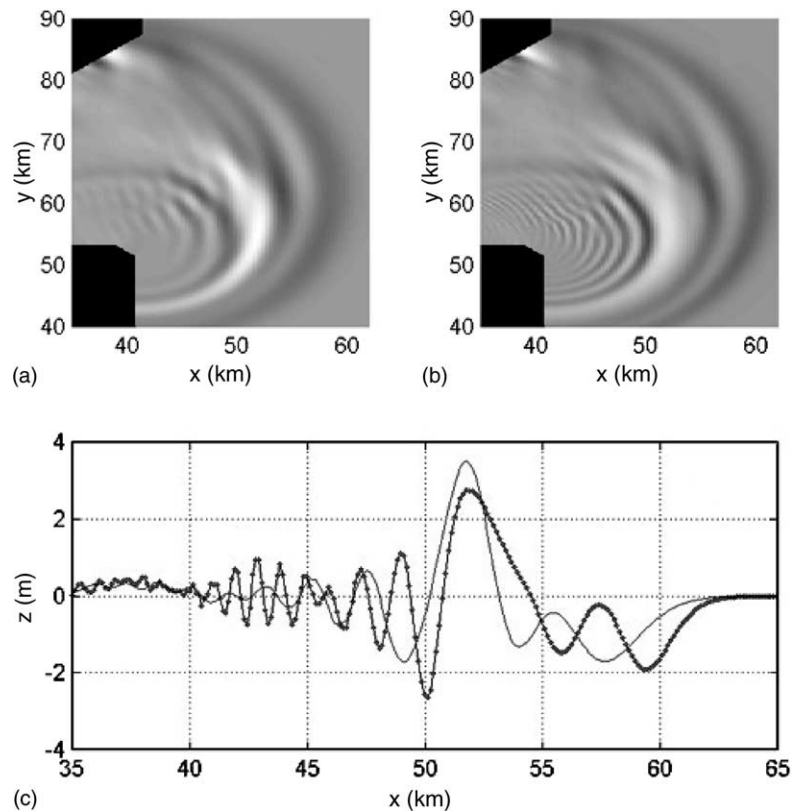


Fig. 7. (a) Numerical snapshot from a linear simulation, and (b) the same snapshot from a nonlinear simulation. Cross sections at $y = 55$ km from the snapshots (a) and (b) are shown in (c), where the dotted line is the nonlinear results and the solid line is the linear profile.

water. At the southern tip of the Strait, there is now a positive elevation wave trailing the lead depression wave, created as the wave shoals in the locally shallower water. At this time the maximum depression of the leading wave has decreased to near 5 m, due to diffraction and dispersion effects. Ten hours into the simulation, shown in Fig. 6(d), the solitary wave has degenerated into a complicated waveform. The leading amplitude has diminished to roughly 2 m (1/10 of the original wave height), and is followed by numerous smaller amplitude and wavelength disturbances.

To demonstrate the effects of nonlinearity, an additional numerical simulation was run utilizing the linear form of the model equations (28) and (29). A snapshot from the linear test, along with the corresponding image from the nonlinear simulation, is shown in Fig. 7. The conclusions drawn from this comparison will be similar to those derived while discussing 1D shoaling (Fig. 4). The nonlinear wave front travels with a greater velocity, and more energy is transferred into the trailing waves, as evident by the greater amplitude. The frequency of the oscillatory trailing waves is much higher in the nonlinear case, by roughly a factor of 2. These steep, high-frequency trailing waves are often captured in satellite imagery, and appear to be dominantly caused by nonlinear interactions.

In Fig. 8 two spatial snapshots are shown, one from the numerical results ($t = 6$ h into simulation) and another taken from a satellite image. The location of images is at the southeastern tip of the Strait, at the entrance to the Mediterranean Sea ($x = 40$ km, $y = 50$ km in Fig. 6). The numerical snapshot presented was chosen based on similarity to the satellite image. Note that the viewing angles of the images are not identical, but the scale and total

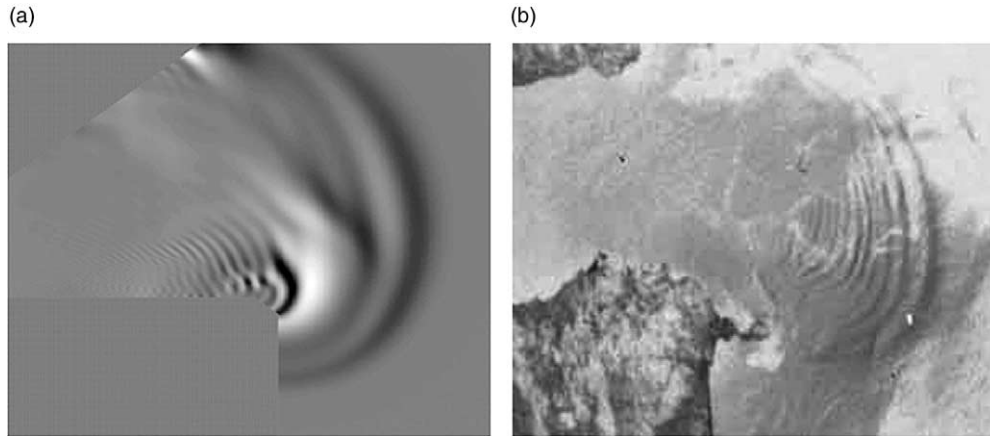


Fig. 8. (a) Numerical snapshot of wave passing through the Strait of Gibraltar, and (b) a satellite image of the same location.

area of the images are similar. The wave fronts are oriented in the same way, and the train of decreasing wavelength waves are represented in both images.

Another location known for internal waves is the south China Sea. In this region there are numerous SAR images showing long wave fronts stretching hundreds of kilometers (see [12]). Internal waves are created due to interactions between outflow from the China Sea and the Kuroshio current, south of Taiwan and north of the Philippines. Traveling to the west, waves encounter nearly no shallow water until reaching the continental shelf of China, save near the small island of Dongsha. As the internal waves travel west and approach Dongsha, shoaling and refraction become dominant processes.

Using the bathymetry near Dongsha, from the Smith and Sandwell database, a solitary wave approaching and interacting with the island is simulated. The lower layer depth is shown in Fig. 9(a); the upper layer depth is 100 m and constant everywhere. For simplicity, the island is modeled as an octagon. At locations where the water depth becomes shallow, notably northeast and northwest of the island, it was necessary to artificially limit the shallowness of the water. The reason for this is that as the internal wave enters this very shallow water, it breaks. Numerically, wave breaking is usually followed by overflow in the program and an end to the simulation. Although breaking on the northern side of the island is likely an important physical process, we seek to eliminate it so that wave interaction behind the island can be investigated. For this reason, the shallowness of the lower layer was limited to 50 m. The initial solitary wave amplitude is 15 m ($\epsilon = 0.18$), located at $x = 58$ km, and traveling in the negative x -direction. Fig. 9(b), taken 9 h after the start of the simulation, shows the wave interacting with the east side of the island. The wave front is irregular, as the shallow water to the north of the island has significantly slowed the wave in this region. Also, part of the wave front has reflected off the east side of the island, and is traveling now to the east. Note that for the most part this reflected wave is a nonphysical result of the manner in which the island is modeled. As shown in experimental studies [21], when internal waves shoal and runup a slope, very little energy is reflected. This difference is expected, as a vertical wall at a finite depth is a poor model for a slope into zero depth.

In Fig. 9(c), 13 h into the simulation, the wave continues to travel past the island, and begins to diffract behind it. By Fig. 9(d), 6 h later, the wave front has completely passed the island, and diffracting waves from the north and south interact. This type of complicated wave–wave interaction pattern can also be seen in the satellite imagery. Fig. 10 shows two images, one numerical (a) and the other satellite (b). The satellite image shows three separate west-moving wave fronts, one significantly before interacting with the island, one immediately before the island, and another behind the island. The numerical image shows the interface displacement of the same wave at three different times, corresponding to similar wave locations in the satellite image, superimposed

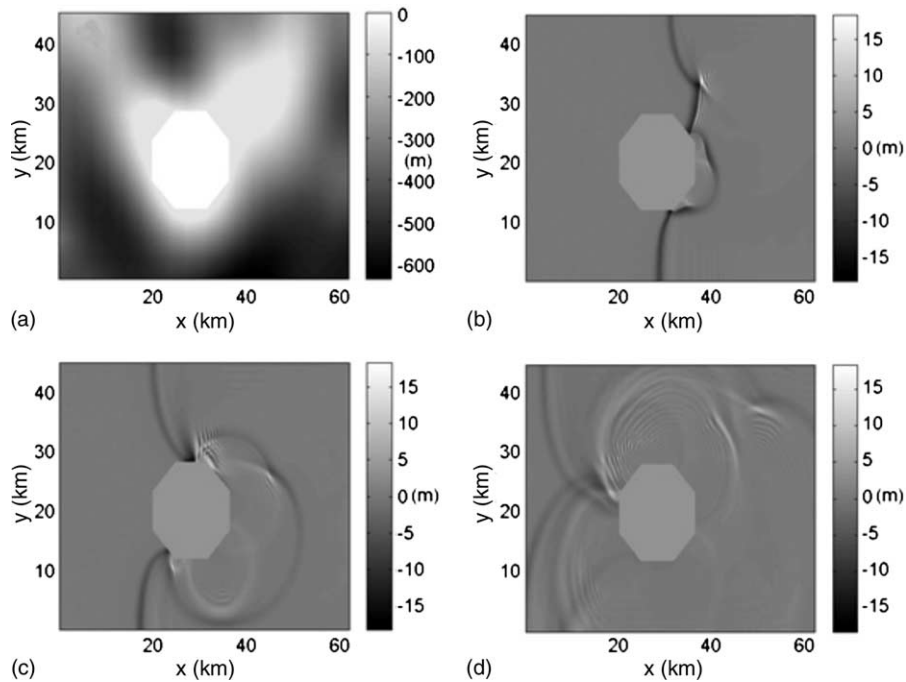


Fig. 9. (a) Numerical simulation of internal wave passing Dongsha Island. Plot (a) shows the lower layer depth profile, and plots (b)–(d) are successive snapshots.

on the same plot. Note that area covered by the numerical image is less than that in the satellite image. The white outline of the island in the numerical image and the black outline of the island in the satellite image are the same physical size. An interesting comparison is the wave field behind the island. The satellite image shows many short wavelength waves obliquely interacting with other waves. The numerical plot shows a similar wave field.

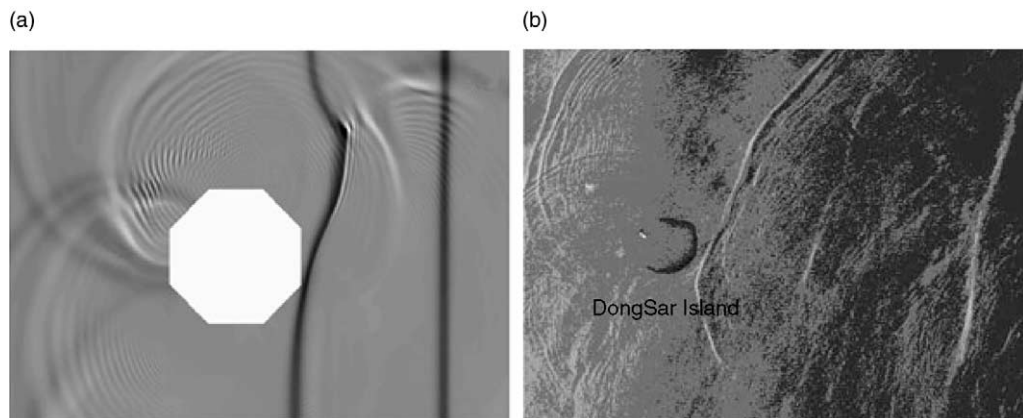


Fig. 10. (a) Overlay of the same numerical wave passing Dongsha Island at three different times, and (b) a satellite image showing three separate internal wave groups.

6. Conclusions

A set of depth-averaged governing equations has been derived for modeling weakly nonlinear and weakly dispersive internal waves. The modeled system consists of a two-layer fluid with a small density difference between the layers. A higher-order nonlinear assumption is made, allowing for the inclusion of both cubic and quadratic nonlinear terms in the governing equations. The numerical predictor–corrector scheme utilizes fourth-order finite differences, and is formally accurate to $(\Delta x)^4$ in space and $(\Delta t)^4$ in time. The numerical model is checked for conservation, permanent analytical solutions, and wave shoaling over a slope–shelf topography. Using real bathymetry, internal wave evolution in the Strait of Gibraltar and wave diffraction around Dongsha Island are simulated. Although there are uncertainties in interpreting the satellite images and in specifying the initial internal waveforms for the numerical model, the results of the numerical simulations show strong similarities with satellite images of the same locations, indicating that the presented model captures two-dimensional and topographical effects. To further advance the modeling of internal wave propagation one needs to parameterize the effects of stratification and energy dissipation due to breaking. Therefore, a higher-order nonlinear model, along with a wave breaking model that can be used by depth-integrated equations, is needed. Accurate field observations and laboratory experimental data are essential for this goal.

Appendix A. Derivation of model equations

Using μ^2 as the small parameter, we can expand the dimensionless physical variables as power series of μ^2 .

$$f = \sum_{n=0}^{\infty} \mu^{2n} f_n \quad (f = p_1, p_2, \mathbf{U}, \mathbf{u}), \tag{A.1}$$

$$q = \sum_{n=1}^{\infty} \mu^{2n} q_n \quad (q = W, w). \tag{A.2}$$

Furthermore, we will adopt the following assumption on the vorticity field. We assume that the vertical vorticity components, $(U_y - V_x)$ and $(u_y - v_x)$, are of $O(1)$, while the horizontal vorticity components are weaker and satisfy the following conditions:

$$\frac{\partial}{\partial z}(\mathbf{U}_0, \mathbf{u}_0) = 0, \tag{A.3}$$

$$\frac{\partial}{\partial z}(\mathbf{U}_1, \mathbf{u}_1) = \nabla(W_1, w_1). \tag{A.4}$$

Consequently, from (A.3), the leading order horizontal velocity components are independent of the vertical coordinate, i.e.

$$\mathbf{U}_0 = \mathbf{U}_0(x, y, t), \quad \mathbf{u}_0 = \mathbf{u}_0(x, y, t). \tag{A.5}$$

Substituting (A.1) and (A.2) into the continuity equations (10) and (13) and the boundary conditions (A.8) and (A.9), we collect the leading order terms as

$$\nabla \cdot \mathbf{U}_0 + W_{1z} = 0, \quad \varepsilon \eta < z < h_1 + \varepsilon \Delta \rho \zeta, \tag{A.6}$$

$$\nabla \cdot \mathbf{u}_0 + w_{1z} = 0, \quad -h_2 < z < \varepsilon \eta, \tag{A.7}$$

$$W_1 = 0 \quad \text{on } z = h_1 + \varepsilon \Delta \rho \zeta, \tag{A.8}$$

$$w_1 = -\mathbf{u}_0 \cdot \nabla h_2 \quad \text{on } z = -h_2. \tag{A.9}$$

Integrating (A.6) and (A.7) with respect to z and using (A.8) and (A.9) to determine the integration constants, we obtain the vertical profile of the following vertical velocity components:

$$w_1 = -z \nabla \cdot \mathbf{u}_0 - \nabla \cdot (h_2 \mathbf{u}_0) = -z Q_0 + R_0, \quad (\text{A.10})$$

$$W_1 = -z \nabla \cdot (\mathbf{U}_0) + h_1 \nabla \mathbf{U}_0 = -z S_0 + T_0, \quad (\text{A.11})$$

where

$$Q_0 = \nabla \cdot \mathbf{u}_0, \quad (\text{A.12})$$

$$R_0 = -\nabla \cdot (h_2 \mathbf{u}_0), \quad (\text{A.13})$$

$$S_0 = \nabla \cdot \mathbf{U}_0, \quad (\text{A.14})$$

$$T_0 = h_1 \nabla \cdot \mathbf{U}_0, \quad (\text{A.15})$$

and Q_0 , R_0 , S_0 , and T_0 are scalar quantities that are functions of x , y , and t .

Similarly, integrating (A.4) with respect to z with information from Eqs. (A.10) and (A.11), we can find the second-order components of the horizontal velocities:

$$\mathbf{U}_1 = -\frac{1}{2} z^2 \nabla S_0 + z \nabla T_0 + \mathbf{C}_1(x, y, t), \quad (\text{A.16})$$

$$\mathbf{u}_1 = -\frac{1}{2} z^2 \nabla Q_0 + z \nabla R_0 + \mathbf{C}_2(x, y, t), \quad (\text{A.17})$$

in which \mathbf{C}_1 and \mathbf{C}_2 are unknown functions to be determined. Up to $O(\mu^2)$, the horizontal velocity components can be expressed as

$$\mathbf{U} = \mathbf{U}_0(x, y, t) + \mu^2 \left\{ -\frac{1}{2} z^2 \nabla S_0 + z \nabla T_0 + \mathbf{C}_1(x, y, t) \right\}, \quad \varepsilon \eta < z < h_1 + \varepsilon \Delta \rho \zeta, \quad (\text{A.18})$$

$$\mathbf{u} = \mathbf{u}_0(x, y, t) + \mu^2 \left\{ -\frac{1}{2} z^2 \nabla Q_0 + z \nabla R_0 + \mathbf{C}_2(x, y, t) \right\}, \quad -h_2 < z < \varepsilon \eta. \quad (\text{A.19})$$

Now, we can define the depth-averaged horizontal velocity vectors, $\bar{\mathbf{U}}(x, y, t)$ and $\bar{\mathbf{u}}(x, y, t)$. Integration of (A.18) and (A.19) through the respective layers and substitution of (A.18) and (A.19) yield the following relationships:

$$\mathbf{U} = \bar{\mathbf{U}} - \mu^2 \left[\left(\frac{1}{2} z^2 - \frac{1}{6} h_1^2 \right) \nabla \bar{S} - \left(\frac{1}{2} h_1 - z \right) \nabla \bar{T} \right] + O(\varepsilon \mu^2, \Delta \rho \varepsilon \mu^2, \mu^4), \quad (\text{A.20})$$

$$\mathbf{u} = \bar{\mathbf{u}} - \mu^2 \left[\left(\frac{1}{2} z^2 - \frac{1}{6} h_2^2 \right) \nabla \bar{Q} - \left(\frac{1}{2} h_2 - z \right) \nabla \bar{R} \right] + O(\varepsilon \mu^2, \mu^4), \quad (\text{A.21})$$

where the scalars \bar{Q} , \bar{R} , \bar{S} , and \bar{T} are defined as

$$\bar{Q} = \nabla \cdot \bar{\mathbf{u}}, \quad (\text{A.22})$$

$$\bar{R} = -\nabla \cdot (h_2 \bar{\mathbf{u}}), \quad (\text{A.23})$$

$$\bar{S} = \nabla \cdot \bar{\mathbf{U}}, \quad (\text{A.24})$$

$$\bar{T} = h_1 \nabla \cdot \bar{\mathbf{U}}. \quad (\text{A.25})$$

Note that $\bar{\mathbf{U}} = \mathbf{U}_0 + O(\mu^2)$ and $\bar{\mathbf{u}} = \mathbf{u}_0 + O(\mu^2)$ have been used in (A.20) and (A.21). Moreover, $O(\varepsilon^3) = O(\mu^4)$ has been employed. The truncation errors due to the different parameters, such as $\Delta \rho$, will be carried through until the end of the derivation, even though they are of identical order to other noted truncations. This is done to make the process of following the derivation, including intermediate steps, easier for the reader.

The pressure field in both fluids must now be determined. This can be accomplished by approximating the vertical momentum equations (12) and (15) as

$$\frac{\varepsilon}{\rho_1} p_{1z} = -\mu^2(\varepsilon W_{1t} + \varepsilon^2 \mathbf{U}_0 \cdot \nabla W_1 + \varepsilon^2 W_1 W_{1z}) + O(\mu^4), \quad \varepsilon\eta < z < h_1 + \varepsilon \Delta\rho \zeta, \quad (\text{A.26})$$

$$\frac{\varepsilon}{\rho_2} p_{2z} = -\mu^2(\varepsilon w_{1t} + \varepsilon^2 \mathbf{u}_0 \cdot \nabla w_1 + \varepsilon^2 w_1 w_{1z}) + O(\mu^4), \quad -h_2 < z < \varepsilon\eta. \quad (\text{A.27})$$

We can integrate the equations above with respect to z and apply the boundary conditions (17) and (18) to find the pressure field as

$$p_1 = \rho_1 \zeta - \mu^2 \rho_1 \left[-\frac{1}{2}(z^2 - h_1^2) \bar{S} + (z - h_1) \bar{T} \right]_t + O(\varepsilon \mu^2, \Delta\rho \varepsilon \mu^2, \mu^4), \quad \varepsilon\eta < z < h_1 + \varepsilon \Delta\rho \zeta, \quad (\text{A.28})$$

$$p_2 = p_{1z=\varepsilon\eta} + \eta - \mu^2 \rho_2 \left[-\frac{1}{2} z^2 \bar{Q} + z \bar{R} \right]_t + O(\varepsilon \mu^2, \mu^4), \quad -h_2 < z < \varepsilon\eta. \quad (\text{A.29})$$

It is noted here that (A.10) and (A.11) have been used in deriving (A.28) and (A.29). To obtain the governing equation for \bar{U} , we substitute (A.20) and (A.28) into (11), yielding the following equation:

$$\bar{U}_t + \varepsilon \bar{U} \cdot \nabla \bar{U} + \nabla \zeta - \mu^2 \left(\frac{1}{3} h_1^2 \right) \nabla \bar{S}_t = O(\varepsilon \mu^2, \Delta\rho \varepsilon \mu^2, \mu^4). \quad (\text{A.30})$$

To obtain the governing equation for \bar{u} , we substitute (A.20) and (A.28) into (11), yielding the following equation:

$$\bar{u}_t + \varepsilon \bar{u} \cdot \nabla \bar{u} + \frac{1}{\rho_2} \nabla(\rho_1 \zeta + \eta) + \mu^2 \left[\frac{h_2^2}{6} \nabla \bar{Q} + \frac{h_2}{2} \nabla \bar{R} \right]_t = O(\varepsilon \mu^2, \Delta\rho \varepsilon \mu^2, \mu^4). \quad (\text{A.31})$$

The above equations are the coupled governing equations, written in terms of \bar{U} , \bar{u} , and η , for weakly nonlinear, weakly dispersive internal waves. At this point, the layer momentum equations are combined. The layer momentum equations are first multiplied by the respective layer density, and then subtracted from each other, giving

$$\begin{aligned} & [\rho_2 \bar{u}_t - \rho_1 \bar{U}_t] + \varepsilon [\rho_2 \bar{u} \cdot \nabla \bar{u} - \rho_1 \bar{U} \cdot \nabla \bar{U}] + \nabla \eta + \mu^2 \left\{ \frac{1}{6} \rho_2 h_2^2 \nabla(\nabla \cdot \bar{u}) - \frac{1}{2} \rho_2 h_2 \nabla[\nabla \cdot (h_2 \bar{u})] \right. \\ & \left. + \mu^2 \left(\frac{1}{3} \rho_1 h_1^2 \right) \nabla(\nabla \cdot \bar{U}) \right\}_t = O(\varepsilon \mu^2, \Delta\rho \varepsilon \mu^2, \mu^4). \end{aligned} \quad (\text{A.32})$$

Note that the momentum flux associated with the change in the free ocean surface, $\nabla \zeta$, cancels out when the two equations are subtracted from one another. Therefore, the variation in the free surface caused by the internal wave propagation has no effect on the internal wave itself, to the order of the derived model equations.

The mass flux in the upper and lower layers can be equated as follows:

$$(h_1 - \varepsilon\eta) \bar{U} = -(h_2 + \varepsilon\eta) \bar{u} + O(\Delta\rho) = \mathbf{M}, \quad (\text{A.33})$$

which is taken directly from (23) and (24). The new variable $\mathbf{M} = (P, Q)$, the lower layer flux, is the variable that the governing equations will be in terms of. Before substitution of (A.33) into the momentum equations (A.32) and (A.33) is expanded in terms of ε :

$$\bar{U} = -\frac{1}{h_1 - \varepsilon\eta} \mathbf{M} = -\frac{1}{h_1} \left(1 + \frac{\varepsilon\eta}{h_1} + \frac{\varepsilon^2 \eta^2}{h_1^2} \right) \mathbf{M} + O(\varepsilon^3, \Delta\rho), \quad (\text{A.34})$$

$$\bar{u} = \frac{1}{h_2 + \varepsilon\eta} \mathbf{M} = -\frac{1}{h_2} \left(1 - \frac{\varepsilon\eta}{h_2} + \frac{\varepsilon^2 \eta^2}{h_2^2} \right) \mathbf{M} + O(\varepsilon^3, \Delta\rho). \quad (\text{A.35})$$

Substituting the above expressions into the momentum equation, along with the assumption $\rho_2/\rho_1 = 1 + O(\mu^4)$ and a great deal of algebra, gives the final momentum equation:

$$\begin{aligned} \mathbf{M}_t + \left(\frac{1}{h_1} + \frac{1}{h_2} \right)^{-1} \nabla \eta + \varepsilon \left(\frac{1}{h_1} - \frac{1}{h_2} \right) [\mathbf{M} \cdot \nabla \mathbf{M} - (\mathbf{M} \eta)_t] - \varepsilon \frac{1}{h_1^3} \left(\frac{1}{h_1} + \frac{1}{h_2} \right)^{-1} [(\mathbf{M} \cdot \nabla h_2) \mathbf{M}] \\ + \varepsilon^2 \left(\frac{1}{h_1^2} - \frac{1}{h_2 h_1} + \frac{1}{h_2^2} \right) [(\mathbf{M} \eta^2)_t - (\mathbf{M} \cdot \nabla)(\eta \mathbf{M}) - \eta (\mathbf{M} \cdot \nabla) \mathbf{M}] + \mu^2 \frac{h_1 h_2}{3} \nabla (\nabla \cdot \mathbf{M}_t) \\ - \mu^2 \left(\frac{1}{h_1} + \frac{1}{h_2} \right)^{-1} \left[(\nabla \cdot \mathbf{M}_t) \nabla \cdot h_2 - \frac{2}{h_2} (\mathbf{M}_t \cdot \nabla h_2) \nabla h_2 + \nabla (\mathbf{M}_t \cdot \nabla h_2) \right] = O(\varepsilon^3, \varepsilon \mu^2, \mu^4, \Delta \rho). \end{aligned} \quad (\text{A.36})$$

Note that according to the assumption that $O(\varepsilon^3) = O(\mu^4)$, the largest of the truncation errors is the $O(\varepsilon \mu^2)$. This term has an equivalent μ error of $O(\mu^{10/3})$, while the other three terms have an equivalent error of $O(\mu^4)$.

References

- [1] T.B. Benjamin, Internal waves of finite amplitude and permanent form, *J. Fluid Mech.* 25 (1966) 241–270.
- [2] C.-Y. Lee, R.C. Beardsley, The generation of long nonlinear internal waves in a weakly stratified shear flow, *J. Geophys. Res.* 79 (1974) 453–462.
- [3] D.M. Farmer, Observations of long nonlinear internal waves in a lake, *J. Phys. Oceanogr.* 8 (1978) 63–73.
- [4] T. Maxworthy, A note on the internal solitary waves produced by tidal flow over a three-dimensional ridge, *J. Geophys. Res.* 84 (1979) 338–346.
- [5] J.R. Apel, J.R. Holbrook, A.K. Liu, J. Tsai, The Sulu Sea internal soliton experiment, *J. Phys. Oceanogr.* 15 (1985) 1625–1651.
- [6] A.K. Liu, Analysis of nonlinear internal waves in the New York Bight, *J. Geophys. Res.* 93 (1988) 122–317.
- [7] S. Pierini, A model for the Alboran Sea internal solitary waves, *J. Phys. Oceanogr.* 19 (1989) 755–772.
- [8] G.G. Tomasson, W.K. Melville, Geostrophic adjustment in a channel: nonlinear and dispersive effects, *J. Fluid Mech.* 241 (1992) 23–57.
- [9] Y. Chen, P.L.-F. Liu, The unified Kadomtsev–Petviashvili equation for interfacial waves, *J. Fluid Mech.* 288 (1995) 383–408.
- [10] W. Choi, R. Camassa, Fully nonlinear internal waves in a two-fluid system, *J. Fluid Mech.* 396 (1999) 1–36.
- [11] P. Brandt, A. Rubing, W. Alpers, J.O. Backhaus, Internal waves in the Strait of Messina studied by a numerical model and synthetic aperture radar images from the ERS 1/2 satellites, *J. Phys. Oceanogr.* 27 (1997) 648–663.
- [12] A.K. Liu, Y.S. Chang, M.-K. Hsu, N.K. Liang, Evolution of nonlinear internal waves in the east and south China Seas, *J. Geophys. Res.* 103 (1998) 7995–8008.
- [13] G. Wei, J.T. Kirby, A time-dependent numerical code for extended Boussinesq equations, *J. Waterway, Port, Coastal Ocean Eng.* 120 (1995) 251–261.
- [14] H.U. Sverdrup, M.W. Johnson, R.H. Fleming, *The Oceans: Their Physics, Chemistry, and General Biology*, Prentice-Hall, Englewood Cliffs, NJ, 1942, pp. 585–588.
- [15] P. Lynett, P.L.-F. Liu, I. Losada, C. Vidal, Solitary wave interaction with porous breakwaters, *J. Waterway, Port, Coastal Ocean Eng.* 126 (6) (2000) 314–323.
- [16] W.H. Press, B.P. Flannery, S.A. Teukolsky, *Numerical Recipes*, Cambridge University Press, Cambridge, 1989, pp. 569–572.
- [17] K.-H. Wang, Diffraction of solitary waves by breakwaters, *J. Waterway, Port, Coastal Ocean Eng.* 119 (1) (1993) 49–69.
- [18] G.G. Tomasson, Nonlinear waves in a channel: three-dimensional and rotational effects, Ph.D. Thesis, Massachusetts Institute of Technology, 1991.
- [19] J.W. Miles, On internal solitary waves, *Tellus* 31 (1979) 456–462.
- [20] K.R. Helfrich, W.K. Melville, On long nonlinear internal waves over slope–shelf topography, *J. Fluid Mech.* 167 (1986) 285–308.
- [21] K.R. Helfrich, Internal solitary wave breaking and run-up on a uniform slope, *J. Fluid Mech.* 243 (1992) 133–154.
- [22] J. Ziegenbein, Spatial observations of short internal waves in the Strait of Gibraltar, *Deep Sea Res.* 17 (1970) 867–875.